Transit spectrophotometry of the exoplanet HD 189733b. I. Searching for water but finding haze with HST NICMOS

D. K. Sing, J. -M. Désert, A. Lecavelier Des Etangs, G. E. Ballester, A. Vidal-Madjar, V. Parmentier, G. Hebrard, G. W. Henry

A&A 505, 891–899 (2009)
DOI: 10.1051/0004-6361/200912776

Astronomy & Astrophysics

Transit spectrophotometry of the exoplanet HD 189733b

I. Searching for water but finding haze with HST NICMOS

D. K. Sing[1], J.-M. Désert[1], A. Lecavelier des Etangs[1], G. E. Ballester[2], A. Vidal-Madjar[1], V. Parmentier[1], G. Hebrard[1], and G. W. Henry[3]

[1] UPMC Univ Paris 06, CNRS, Institut d'Astrophysique de Paris, 98bis boulevard Arago, 75014 Paris, France
e-mail: sing@iap.fr
[2] Lunar and Planetary Laboratory, University of Arizona, Sonett Space Science Building, Tucson, AZ 85721-0063, USA
[3] Center of Excellence in Information Systems, Tennessee State University, 3500 John A. Merritt Blvd., Box 9501, Nashville, TN 37209, USA

Received 29 June 2009 / Accepted 27 July 2009

ABSTRACT

We present Hubble Space Telescope near-infrared transit photometry of the nearby hot-Jupiter HD 189733b. The observations were taken with the NICMOS instrument during five transits, with three transits executed with a narrowband filter at 1.87 μm and two performed with a narrowband filter at 1.66 μm. Our observing strategy using narrowband filters is insensitive to the usual HST intra-orbit and orbit-to-orbit measurement of systematic errors, allowing us to accurately and robustly measure the near-IR wavelength dependance of the planetary radius. Our measurements fail to reproduce the previously claimed detection of an absorption signature of atmospheric H_2O below 2 μm at a 5σ confidence level. We measure a planet-to-star radius contrast of 0.15498 ± 0.00035 at 1.66 μm and a contrast of 0.15517 ± 0.00019 at 1.87 μm. Both of our near-IR planetary radii values are in excellent agreement with the levels expected from Rayleigh scattering by sub-micron haze particles, observed at optical wavelengths, indicating that upper-atmospheric haze still dominates the near-IR transmission spectra over the absorption from gaseous molecular species at least below 2 μm.

Key words. planetary systems – stars: individual: HD 189733 – techniques: photometric – binaries: eclipsing

1. Introduction

Transiting close-in exoplanets have provided the extraordinary possibility to begin studying the detailed characteristics of extrasolar planets. A transit or anti-transit event allows for an exoplanet to be temporally resolved from the bright parent host star, isolating such valuable information as the planet's absorption or emission spectra. During a primary transit event, both the opaque body of the planet as well as its atmosphere blocks light from the parent star. A precise determination of the radius of the planet can be made from the total obscuration, while partial transmission of light through the exoplanet's atmosphere, with its wavelength and altitude dependence, allows for detecting composition and structure. The frequent transits, anti-transits, and large signals make hot Jupiters the best targets for these studies. Space-based observatories, notably HST and Spitzer, have proven to be extremely efficient platforms on which to do follow-up transit and anti-transit studies given their superior photometric performance, wide wavelength range, and ability to observe multiple transits over long baselines within a single observing season.

Two hot Jupiters in particular, HD 189733b and HD 209458b, currently offer the very best laboratories in which to study exoplanet atmospheres and have become the prototype hot-Jupiter planets. These two planets have the brightest parent stars among transiting planets and have large transit depths, making precise studies at high signal-to-noise ratios possible. The first transiting planet discovered, HD 209458b, holds the distinction of the first detection of an extrasolar planetary atmosphere (Charbonneau et al. 2002) and escaping atmosphere (Vidal-Madjar et al. 2003, 2004, 2008; Ballester et al. 2007). The optical transmission spectra of this planet shows evidence for several different layers of Na (Sing et al. 2008a,b) as well as Rayleigh scattering by molecular hydrogen (Lecavelier des Etangs et al. 2008b) and the presence of TiO/VO (Désert et al. 2008). The atmospheric Na signature has also been confirmed by ground based observations (Snellen et al. 2008). This planet also exhibits a stratospheric temperature inversion (Burrows et al. 2007; Knutson et al. 2008) thought to be caused by a strong optical absorber such as TiO (Désert et al. 2008; Hubeny et al. 2003; Fortney et al. 2008) and/or HS and S_2 (Zahnle et al. 2009).

HD 189733b (Bouchy et al. 2005; Hébrard & Lecavelier Des Etangs 2006) is among the closest known transiting planets with a K1.5V type parent star, giving it one of the largest transit and anti-transit signals known. Spitzer anti-transit measurements have shown efficient heat redistribution, measuring the planet's temperature profile from orbital phase curves (Knutson et al. 2007, 2009) and a definitive detection of atmospheric water from emission spectra (Grillmair et al. 2008). The signature of CO_2 has also been seen from HST/NICMOS emission spectra (Swain et al. 2009). In primary transit, Pont et al. (2008) used the ACS grism to provide the first transmission spectra from 0.6 to 1.0 μm. This spectrum is seen to be almost featureless likely indicating the presence of high altitude haze, with a λ^{-4} wavelength dependence of the spectra likely due to Rayleigh scattering by sub-micron $MgSiO_3$ molecules (Lecavelier des Etangs et al. 2008a). From the ground, Redfield et al. (2008) detected

strong Na absorption in the core of the doublet. In the infrared, Swain et al. (2008) used HST/NICMOS and showed evidence for absorption of atmospheric water and methane while Spitzer broadband transit photometry has given evidence for CO (Désert et al. 2009a).

The current transmission spectrum of HD 189733b appears to be one which is dominated by condensed haze particles in the optical, but dominated by the absorption of gaseous molecular species (e.g., H_2O, CO, CH_4) at near-infrared and infrared wavelengths. The transition wavelength between being dominated by haze or gaseous species should give indications of the particle size of the condensed haze, though it is not clear if all the current observations are completely compatible and can give a coherent picture of the planet's atmosphere.

Here we present near-infrared HST photometry of HD 189733b during five transits, designed with the intended goal of measuring the signature of atmospheric water. This work is part of our ongoing efforts to charaterize the transit spectra of HD 189733 using space-based observatories (Désert et al. 2009a,b). We observed with two narrowband filters and designed the observing program to be unbiased from the typical orbit-to-orbit and intra-orbit systematic errors inherent in observing in spectroscopic modes with HST STIS, ACS (e.g., Brown et al. 2001; Pont et al. 2007) and NICMOS (e.g., Swain et al. 2008; Carter et al. 2009) instruments. In Sects. 2 and 3, we detail these observations, which include correcting for the presence of unocculted star spots and stellar limb darkening. In Sect. 4 we present the analysis of our transit light curves and discuss our results in Sects. 5 and 6.

2. Observations

2.1. Hubble space telescope NICMOS narrowband photometry

We observed HD 189733 during five transits using the Near Infrared Camera and Multi Object Spectrometer (NICMOS) aboard the Hubble Space Telescope during Cycle 16 (GO-11117). Each transit observation consisted of four consecutive spacecraft orbits, each roughly centered on a transit event. The visits occurred during: 15 April 2008 UT 15:36 to 21:17 for visit #1; 3 May 2008 UT 08:51 to 14:26 for visit #2; 18 May 2008 UT 22:44 to 19 May 2008 UT 04:27 for visit #3; 25 May 2008 UT 14:33 to 20:15 for visit #4; and 11 Aug 2008 UT 06:24 to 12:04 for visit #5. For each transit event, we obtained images using the high resolution NIC1 camera with only a single narrowband filter, using either the $F166N$ filter centered at 1.6607 μm ($\Delta\lambda$ = 0.0170 μm) or the $F187N$ filter centered at 1.8748 μm ($\Delta\lambda$ = 0.0191 μm). By not switching between filters, the duty cycle of the instrument is increased as much less overhead time is spent between consecutive exposures.

The NICMOS instrument has three 256 × 256 pixel HgCdTe actively cooled cameras with the NIC1 camera offering the highest spatial resolution, having a 11 × 11 arcsec field of view and 43 milliarsec sized pixels. The high resolution of the camera combined with the use of narrowband filters allowed us to observe the bright (V_{mag} = 7.67) star with short 2–4 s exposures well before saturating the detector. We also adopted a modest defocus during our observations, such that the photometry would be more insensitive to flat fielding errors and sub-pixel variations. The $F187N$ filter images were taken in Multiaccum SPARS4 mode with Nsamp=3 yielding 4.00 s exposures while the $F166N$ filter images were taken with Multiaccum STEP1 mode with Nsamp=4 yielding 1.99 s exposures. Both observing modes have a 9 s readout overhead. In visit #1 we obtained 793 F187N exposures, in visit #2 860 F166N exposures, in visit #3 418 F187N exposures, in visit #4 927 F166N exposures, and in visit #5 751 F187N exposures. The data quality of visit #3 was compromised by a failure of a known 2-gyro issue with the Fixed Head Star Trackers. The failure caused a total loss of the visit #3 out-of-transit data. However, even without a long out-of-transit baseline flux, visit #3 still proved useful when analyzing the data in conjunction with the other two F187N visits.

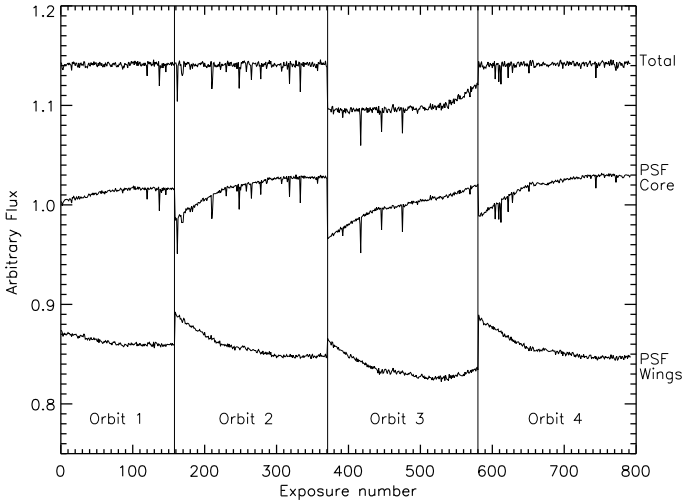

Fig. 1. Aperture photometry from Visit #1 using the F187N narrowband filter. The data from all four spacecraft orbits of the HST visit are plotted back-to-back (there are ~45 min data gaps between HST orbits due to Earth occultation). The transit occurs in orbit 3 between exposures 371 and 580 and is visible in the top plot. Plotted are the total counts from a 15.2 pixel aperture (*top*), along with the counts from only the PSF central core (*middle*, 4.25 pixel aperture), and counts from only the PSF wings containing the 1st and 2nd airy rings (*bottom*, ring with inner-annulus of 4.25 pixels outer-annulus 15.2 pixels). The intra-orbit thermal focus variations change the shape of the PSF during an orbit, which can be seen by the large flux changes in counts of the PSF core and wings. However, with our narrowband filters the total counts are conserved in wide apertures, which exhibit no residual intra-orbit variations. A small intrapixel sensitivity related error is observed in the PSF core photometry which contaminates ~10% of the exposures (see text).

During each HST visit, we obtained 50 exposures in one filter during the beginning of the first orbit, before switching to the opposite narrowband filter in which the rest of the visit, including the transit, was observed. This short set of opposite-band images was used to help monitor the stellar activity, such that the absolute flux and activity level of the star would be known at each of our two wavelengths for all five visits.

We performed aperture photometry on the calibrated STScI pipeline reduced images. The pipeline includes corrections for bias subtraction, dark current, detector non-linearities, and applies a flat field calibration. The aperture location for each image was determined using a two dimensional Gaussian fit of the point spread function (PSF) for each image. We found apertures with a radii of 15.2 pixels for the $F187N$ filter and 14.7 pixels for the $F166N$ filter minimized the standard deviation of the out-of-transit light curves. The background in our short exposures was found to be negligible, typically accounting for only ~50 total counts per image.

Our choice of a wide aperture minimizes the effect of intra-orbit thermal focus variations (see Fig. 1). This well known

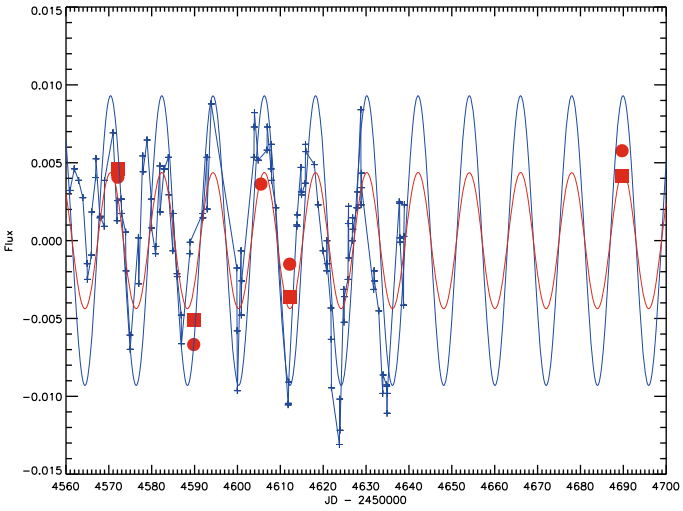

Fig. 2. Simultaneous ground-based photometric monitoring of HD 189733 (blue crosses) continued from Henry & Winn (2008), along with a fitted sinusoid (blue). The NICMOS flux levels for all five visits are also plotted for both the $F166N$ filter (red squares) and the $F187N$ filter (red dots). Assuming 1000 K cooler star spots with ~2% coverage, the amplitude of the near-IR spot modulation is expected to be about half that observed in the optical (red sinusoid). The NICMOS flux levels are seen to modulate in phase with the optical ground-based data at approximately the expected near-IR spot amplitude.

effect (see STScI Instrument Science Reports ACS2008-03[1] and NICMOS ISR2007-003[2]) changes the shape of the PSF during an orbit and is due to small changes in the focus of the telescope, which are ascribed to temperature variations. With a sufficiently wide aperture, covering at least the central peak and first and second airy rings, no residual intra-orbit variations are observed. In four of our five orbits, the photometric time series exhibit sudden drops in flux, confined to the central core of the PSF and effects 10–15% of the images. We attribute this phenomenon to a likely intrapixel sensitivity variation, as it is confined to pixels in the central PSF core which have the largest change in flux across a pixel and the effect is smaller for higher levels of defocus. Images which show this intrapixel sensitivity effect were easily flagged by comparing the photometric time series of the photometry of the central PSF core to the photometry of the outer-airy rings, which are insensitive to the effect (see Fig. 1). We adopted two strategies to deal with these flagged images, choosing to either eliminate them from the remaining analysis or interpolate the affected PSF core photometry using neighboring images in the time series. Both methods produced equivalent results in the final transit light curve fits. We note that future HST/NICMOS programs can eliminate this small problem completely by adopting a larger defocus, as is the case here in visit #5 which does not exhibit this effect.

2.2. Monitoring the stellar activity

We monitored the stellar activity of HD 189733 using both ground-based data and the absolute flux level from the NICMOS instrument itself. The ground-based coverage was provided by the T10 0.8 m Automated Photoelectric Telescope (APT) at Fairborn Observatory in southern Arizona. This ongoing observing campaign of HD 189733 began in October 2005 and is detailed in Henry & Winn (2008). The APT uses two photomultiplier tubes to simultaneously gather Stromgren b and y photometry. The APT data spans four of our five HST visits (see Fig. 2), with only the fifth visit not covered as the telescope is shut down during the Arizona monsoon season. This dataset also covers the HD 189733 stellar activity during the epochs of the HST transmission spectra from Pont et al. (2007) and Swain et al. (2008) as well as the Spitzer transit photometry of Désert et al. (2009a), Désert et al. (2009b), and Knutson et al. (2009) making it an invaluable resource when comparing the stellar activity level from epoch to epoch.

The near-IR flux levels for HD 189733, during our five visits, are based on the baseline flux level from each transit light curve as well as the first 50 exposures obtained in the filter opposite to that of the transit (i.e. F166N or F187N). While these first 50 exposures were obtained during the first orbit of a visit, these orbits did not show any significant signs of systematic errors. Our use of the first orbit is in contrast to nearly all previous similar HST studies (including the STIS and NICMOS instruments), which have had to disregarded the first orbit of an HST visit. During the first orbit, the telescope thermally relaxes in its new pointing position causing significant flux variations. The near-IR stellar flux levels are shown in Fig. 2, with an arbitrary zero-magnitude flux, which clearly modulate in phase with the optical measurements.

3. Stellar limb darkening

3.1. Three parameter non-linear limb-darkening law

For solar-type stars at near-infrared and infrared wavelengths, the strength of stellar limb darkening is weaker compared to optical wavelengths. However, the intensity distribution is increasingly non-linear at these longer wavelengths (see Fig. 5 of Sing et al. 2008a), which can require adopting non-linear limb-darkening laws when fitting high S/N transit light curves. Many studies have chosen to use a quadratic or four parameter non-linear limb-darkening law to describe the stellar intensity distribution (Claret 2000), with the coefficients determined from stellar atmospheric models. As noted by Sing et al. (2008a) for the widely used Kurutz 1D ATLAS stellar models, the largest differences between existing limb-darkening data and the 1D stellar models is at the very limb, where ATLAS models predict a dramatic increase in the strength of limb darkening. For the sun, the ATLAS models over-predict the strength of limb darkening by >20% at $\mu = \cos(\theta)$ values below 0.05, though they perform well otherwise. Both solar data (Neckel & Labs 1994) and 3D stellar models (Bigot et al. 2006) show the intensity distribution at the limb to vary smoothly to $\mu = 0$, with no dramatic or sudden increases in limb-darkening strength. To mitigate this limb effect, we choose to fit for the limb-darkening coefficients from ATLAS models using only values of $\mu \geq 0.05$. We also choose to fit a three parameter non-linear limb-darkening law,

$$\frac{I(\mu)}{I(1)} = 1 - c_2(1-\mu) - c_3(1-\mu^{3/2}) - c_4(1-\mu^2) \quad (1)$$

as the $\mu^{1/2}$ term from the four parameter non-linear law mainly affects the intensity distribution at small μ values and is not needed when the intensity at the limb is desired to vary linearly at small μ values. Compared to the quadratic law, the added $\mu^{3/2}$ term provides the flexibility needed to more accurately reproduce the stellar model atmospheric intensity distribution at near-infrared and infrared wavelengths.

[1] http://www.stsci.edu/hst/acs/documents/isrs/
[2] http://www.stsci.edu/hst/nicmos/documents/isrs/

Table 1. Three parameter non-linear limb darkening coefficients.

Coefficient	$F166N$ filter	$F187N$ filter
c_2	2.1483	1.9508
c_3	−2.7763	−2.4507
c_4	1.1265	0.9770

3.2. HD 189733 limb darkening

The limb-darkening coefficients for the three parameter non-linear law were computed using a Kurucz ATLAS stellar model[3] with $T_{\rm eff}$ = 5000 K, log g = 4.5, and [Fe/H] = 0.0 in conjunction with the transmission through our two narrowband filters. For reasons described above, we fit for the limb-darkening coefficients using the calculated intensities between μ = 0.05 and μ = 1, providing the coefficients in Table 1.

4. Reduction and analysis

4.1. Correcting for non-occulted stellar spots

A transit light curve is affected by the presence of star spots, both when a spot is occulted by the planet and by the presence of non-occulted spots during the epoch of the transit observations (Pont et al. 2008). We will focus on non-occulted spots here, as there is no evidence for occulted spots in any of our observed transit light curves.

Non-occulted stellar spots affect the shape of a transit light curve by making the stellar surface dimmer than a spot-free stellar disk. During transit, the planet hides a larger fraction of the total overall flux, thereby increasing the apparent size of the planet. A wavelength dependance is also introduced, as the stellar flux lost by the spots at a given wavelength will depend on the blackbody temperature difference between the stellar surface and the spots. The stellar spots also create a quasi-periodic photometric variability, as the spots rotate into and out of view at the stellar rotation period.

To correct for the presence of non-occulted stellar spots in this program, we used the ongoing ground-based photometric monitoring data of Henry & Winn (2008) as well as the calibrated flux level of the NICMOS observations, measuring the flux variation due to stellar spot modulation. HD 189733 is an active star, varying in the optical at the 2–3% level with spot-coverage at any given epoch covering ∼1–2% of the stellar surface. The NICMOS observations vary by ∼1% (see Fig. 2), which is consistent with the expected near-IR variation due to stellar spots as it occurs both in phase with the ground-based photometric monitoring and near the amplitude expected when assuming ∼4000 K spot temperatures as measured by Pont et al. (2008) and the observed optical spot coverage. Furthermore, for each visit both the $F166N$ and $F187N$ filters showed similar near-IR stellar flux variations, as would be expected for stellar spots. The baseline flux of each visit was corrected in a differential manner, adding the necessary flux to each visit such that all the observations are compared at the same minimum spot activity baseline flux level. HST visits #1 and #5 occurred at a spot activity minimum, and were chosen here as the flux reference for the remaining visits. The corresponding effect on the final determined radius is somewhat small but these corrections are important as exoplanetary atmospheric signatures are typically also small. An estimated ∼0.0015 uncertainty on the absolute flux level of each visit translates into a spot-correction uncertainty of ∼0.0001 $R_{\rm pl}/R_\star$ and ∼0.25σ on the final values of $R_{\rm pl}/R_\star$ for the two wavelengths when combining the different visits.

[3] http://kurucz.harvard.edu/

4.2. Transit light curve fits

We modeled the transit light curve with the theoretical transit models of Mandel & Agol (2002). We choose to fix the planetary orbital phase using the ephemeris of Knutson et al. (2009) (P = 2.21857578 ± 0.00000080 days; $T_{\rm c}$ = 2454399.23990 ± 0.00017 HJD), fitting for the planet-to-star radius contrast $R_{\rm pl}/R_\star$, the inclination i, and the mean stellar density $\rho_\star$, which is proportional to the system scale ($a/R_\star$) cubed. No significant deviations from the Knutson et al. (2009) ephemeris were found, with the three F187N visits determined to be within 2 s of the predicted central transit time. To account for the effects of limb-darkening on the transit light curve, we adopted the three parameter limb-darkening law and let the linear coefficient, c_2, free in the fit, while c_3 and c_4 were fixed to the best-fit model values listed in Table 1. Choosing to fit only one limb-darkening parameter ensures that the fits are both not significantly biased by adopting a stellar atmospheric model and do not suffer from degeneracies between fitting multiple limb-darkening parameters. We also allowed the flux level of each visit to vary in time linearly, described by two fit parameters. The linear trend accounted for any possible detector drifts or stellar activity related flux variations during the observations and we found that visits #4 & 5 exhibited a small slope. The best fit parameters were determined simultaneously with a Levenberg-Marquardt least-squares algorithm using the unbinned data (see Table 2), with the error of each datapoint set to the standard deviation of the out-of-transit residuals of a given visit.

The fit values for the linear limb-darkening coefficients are consistent within 1σ of the model values (see Table 2). We also performed fits letting either c_3 or c_4 free, with c_2 fixed, finding similar results indicating that the Atlas models are performing well. As a check of our choice adopting the three parameter law, we also fit the four-parameter limb-darkening law fixing c_2, c_3, and c_4 to their model values and letting the c_1 coefficient (proportional to $\mu^{1/2}$) free. At both 1.66 and 1.87 μm, we found c_1 to be consistent with zero. In addition, we tried fits with the quadratic limb-darkening law fitting both coefficients in a minimally correlated fashion (Pál 2008), finding equivalent transit parameters, though the three-parameter law still produced the best χ^2 fits.

Given the accumulating high precision transit data on HD 189733 with both HST and Spitzer, several orbital system parameters (such as i, b, and $a/R_\star$) can be determined more precisely than with just these HST/NICMOS transit observations alone. Transit-fit values for $R_{\rm pl}/R_\star$ are correlated to these system parameters, which can adversely affect a proper comparison of the planetary radii across different wavelengths, when searching for atmospheric signatures, if significantly deviant values are used. Therefore, it is advantageous to fit for $R_{\rm pl}/R_\star$ using the best system parameters available, and also necessary that the parameters are consistent across different studies when comparing the planetary radii between multiple observations. In Fig. 3, we plot the measured orbital system parameters of HD 189733 from Pont et al. (2007), Désert et al. (2009a), Désert et al. (2009b), Knutson et al. (2009), Winn et al. (2007), and this work using the individual NICMOS fits. The results for i, $a/R_\star$, b, and $\rho_\star$ nearly all agree at the ∼1σ level. A notable exception is the 3.6 μm and 5.8 μm Spitzer results from Désert et al. (2009a), which show significantly deviant values in both b and $a/R_\star$. These deviant

Table 2. System parameters of HD 189733b.

Parameter	Individual NICMOS Fits		Joint HST & Spitzer†	
	*F*166*N* filter	*F*187*N* filter	*F*166*N* filter	*F*187*N* filter
central wavelength, λ (μm)	1.6607	1.8748		
wavelength range, $\Delta\lambda(\mu m)$	0.0170	0.0191		
planet-to-star radius contrast, $R_{pl}/R_\star$	0.15464 ± 0.00051	0.15496 ± 0.00028	0.15498 ± 0.00035	0.15517 ± 0.00019
inclination, i (deg)	85.75 ± 0.13	85.715 ± 0.076	85.723 ± 0.024†	
system scale, $a/R_\star$	8.871 ± 0.095	8.854 ± 0.062	8.898 ± 0.027†	
impact parameter, $b = a\cos i/R_\star$	0.657 ± 0.021	0.661 ± 0.013	0.6x636 ± 0.0031†	
stellar density, $\rho_\star$ (g cm^{-3})	2.684 ± 0.086	2.669 ± 0.056	2.709 ± 0.025†	
linear limb-darkening coefficient, c_2	2.195 ± 0.058	1.972 ± 0.029	2.1483	1.9508

† System parameter values and 1-σ error derived from the weighted mean using: Pont et al. (2007) HST/ACS, Désert et al. (2009a,b) Spitzer/IRAC, Knutson et al. (2009) Spitzer/IRAC, and the individual fits of this work HST/NICMOS. The mean value was adopted for the fits.

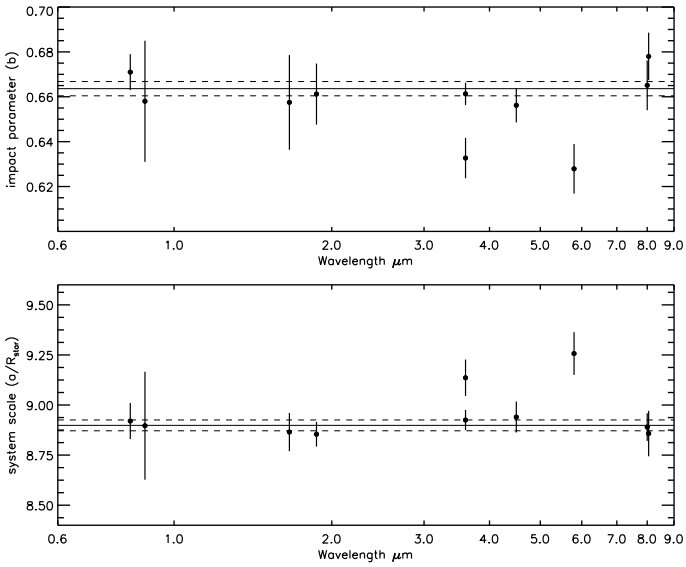

Fig. 3. The impact parameter (*top*) and system scale parameter (*bottom*) vs. wavelength for HD 189733 as measured by Désert et al. (2009a), Désert et al. (2009b), Knutson et al. (2009), Pont et al. (2007), Winn et al. (2007), and this work. Excluding two deviant Spitzer values from Desert et al. (2009; see also Paper II Désert et al. 2009b, for further details), there is a good general agreement between the various HST, Spitzer, and ground-based results with a mean b value of 0.6636 ± 0.0031 and mean $a/R_\star$ value of 8.898 ± 0.027. These mean values are over-plotted (horizontal line) along with their 1σ errors (dashed vertical lines) and adopted for our final transit light curve fits seen in Figs. 5 and 6.

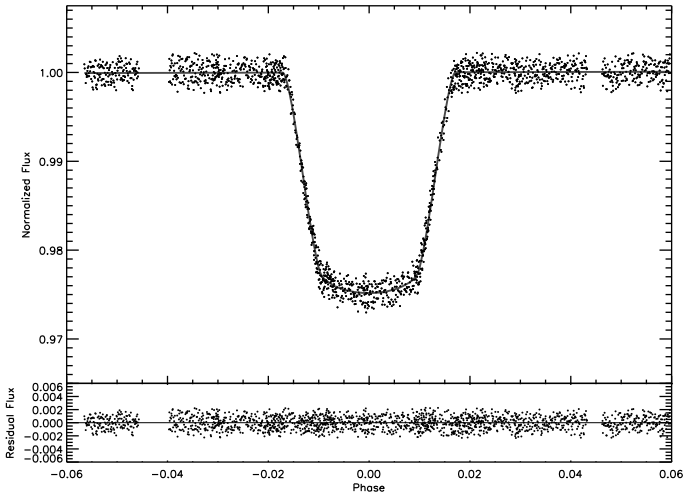

Fig. 4. NICMOS filter transit photometry of all three visits using the 1.8748 μm narrowband filter. The best-fit transit light curve model is also fit (grey) along with the observed-calculated residuals of the fit (*bottom panel*). The light curve has a S/N of 1000 per-point and an equivalent precision of 4.0×10^{-4} in an 80 s bin.

values may have been the result of occulting stellar spots during ingress or egress and were disregarded in this study (see Desert et al. 2009b, for further details). From the HST, Spitzer, and ground-based studies, we derived mean orbital system parameter values calculating a weighted mean using the different measurements. The determined mean values and their associated error are listed in Table 2. These values have an improved determination of i, b, $\rho_\star$ and $a/R_\star$ by up to a factor of seven compared to our individual NICMOS fits and were adopted for our final transit light curve fits (labeled *Joint HST & Spitzer* in Table 2 and plotted in Figs. 4 and 5). We also choose to adopt the model limb-darkening values from Table 1 for the three coefficients, minimizing the number of free fit parameters.

4.3. Red noise estimation

The rms of the residuals between the best-fitting Joint HST & Spitzer models and the data are 9.98×10^{-4} for the $F187N$ filter and 1.67×10^{-3} for the $F166N$ filter. These values are approximately 1.5 times the calculated pipeline error, which is dominated by photon noise. This is a modest improvement over other similar NICMOS transit studies (Carter et al. 2009; Pont et al. 2009), which have generally found 2–3 times the photon noise limit. We checked for the presence of systematic errors correlated in time ("red noise", Pont et al. 2006) using two methods. We first checked that the binned residuals followed a $N^{-1/2}$ relation when binning in time by N points. The presence of red noise causes the variance to follow a $\sigma^2 = \sigma_w^2/N + \sigma_r^2$ relation, where σ_w is the uncorrelated white noise component while σ_r characterizes the red noise. We found no significant evidence for red noise in either the F187N data or F166N data, when binning on timescales up to the ingress and egress duration. We also used the "prayer-bead" method to check for red noise, which consists of a residual permutation algorithm (Moutou et al. 2004). In this method, the residuals of the best-fit model are shifted with wraparound over the light curve and a new fit is performed.

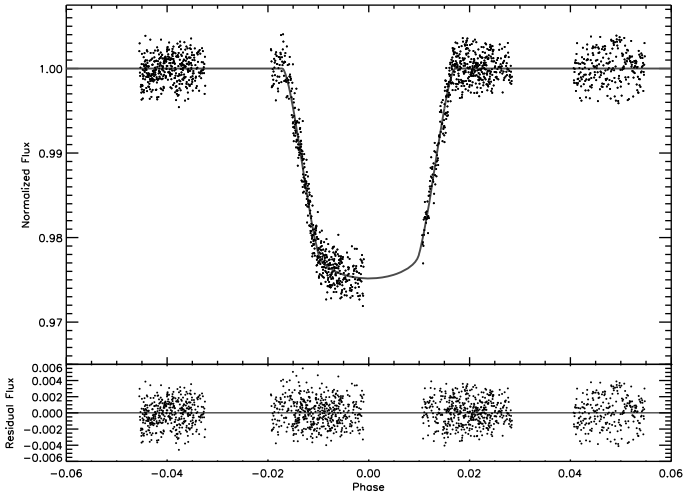

Fig. 5. NICMOS filter transit photometry of both visits using the 1.6607 μm narrowband filter. The best-fit transit light curve model is also fit (grey) along with the observed-calculated residuals of the fit (*bottom panel*). The light curve has a S/N of 600 per-point and an equivalent precision of 6.3×10^{-4} in an 80 s bin.

The structure of any time correlated noise is preserved and its effect on the uncertainty of the transit light curve parameters are revealed in the distribution of fit parameters. The prayer-bead method also showed no significant signs of red noise, as the distribution of each of the fit parameters at both wavelengths were compatible with the uncertainties found from standard χ^2 statistics. With no detectable red noise, our S/N levels are comparable to other high S/N transit light curves, with precisions of 4.0×10^{-4} per 80 s bin for F187N and 6.3×10^{-4} per 80 s bin for F166N.

5. Discussion

5.1. Expected H_2O atmospheric signature

We have presented high signal-to-noise near-infrared transit narrowband photometry of HD 189733 at 1.66 and 1.87 μm, with the intent of searching for a transit signature of atmospheric water. If atmospheric H_2O were the dominant absorbing species at both of these wavelengths, we could expect significant radii differences as H_2O has a strong absorption bandhead over the probed wavelength range. The expected difference in radii can be estimated using the difference between opacities at 1.66 μm and 1.87 μm. We calculate the effective absorption cross sections per molecule to be $\sigma_{1.66} = 8.54{\times}10^{-24}$ and $\sigma_{1.87} = 1.79{\times}10^{-21}$ (cm^2 molecule^{-1}), respectively, using the high temperature line list of Barber et al. (2006), a Voigt broadening line profile, a temperature of 1200 K, and the response through our two narrowband filters. The variation in apparent planetary radius then follows from Eq. (2) of (Lecavelier des Etangs et al. 2008a) giving,

$$\Delta R_{\rm p} = H \ln \frac{\sigma_{1.87}}{\sigma_{1.66}}, \qquad (2)$$

where H is the atmospheric scale height. H is given by $H = kT/\mu g$, where μ is the mean mass of the atmospheric particles taken to be 2.3 times the proton mass, T the temperature, and g the surface gravity. Assuming $R_\star = 0.766\ R_\odot$, $R_{\rm pl} = 1.155\ R_{\rm Jup}$, $M_{\rm pl} = 1.144\ M_{\rm Jup}$, and a temperature of 1200 K, we find $H/R_\star = 0.00038$ which gives an expected radius difference of 0.0020 $R_{\rm pl}/R_\star$. Our HST NICMOS observations show only a radius contrast of $0.00019 \pm 0.00040\ R_{\rm pl}/R_\star$ between the two wavelengths, a factor of 10 lower and 4.6σ away from the expected value. If H_2O was the dominant opacity source in HD 189733b's atmosphere at these altitudes, it would have been easily detected by our observations.

5.2. Comparisons with previous results

Swain et al. (2008) used HST NICMOS to produce a near-IR low resolution grism transmission spectrum of HD 189733b, which appears to show two strong atmospheric features at H_2O and CH_4. This grism spectrum encompasses our wavelength range (see Fig. 6) and appears to show a strong H_2O absorption molecular bandhead feature between 1.5 and 2.0 μm. Between 1.66 and 1.87 μm, Swain et al. (2008) found a radii contrast of $0.00233 \pm 0.00035\ R_{\rm pl}/R_\star$. This radii contrast is significantly larger than the one we observe, with our results failing to reproduce the Swain et al. value at a 5σ confidence level.

Given the large disagreement between our results and Swain et al. (2008), we find two scenarios that could possibly explain the conflicting results. Either the planet's transmission spectrum is variable, or residual systematic errors still plague the edges of the Swain et al. spectrum. Both Swain et al. (2008) and our results correct for stellar starspot activity, ruling out stellar variability as the underlying cause. In addition, the discrepancy between the two results is too large to attribute to random statistical fluctuations. Variability in the planet's transmission spectrum by dynamic weather processes would seem a plausible scenario, especially given the seemingly variable emission spectrum results from Spitzer (Grillmair et al. 2007, 2008). However, we find the transmission variability scenario difficult to substantiate, particularly with the large systematic errors inherent with NICMOS grism observations, which can compromise precision photometric work. In order for the variability scenario to be viable, the optically thick absorbing haze would have to clear out of the atmosphere, over the entire limb, down to altitudes at least 6.7 scale heights lower (~1200 km) to reveal the full extent of the H_2O feature. The haze would also have to clear for only the single epoch of the Swain et al. (2008) HST visit, but not during the seven epochs of the HST visits between Pont et al. (2008) and this work. Likely, the variability scenario is also dependent upon the haze composition, and the transmission spectrum would be difficult to vary with non-condensate Rayleigh scattering candidates such as H_2 (Lecavelier des Etangs et al. 2008a). We note that in our HST visits spanning five months, no significant visit-to-visit planet radius differences were observed at either wavelength, after correction for non-occulted stellar spots. At 1.66 μm we find radii of 0.1545 ± 0.0004 and $0.1551 \pm 0.0006\ R_{\rm pl}/R_\star$ for visits #2 and 4, respectively, while at 1.88 μm we find radii of 0.1549 ± 0.0003 and $0.1558 \pm 0.0004\ R_{\rm pl}/R_\star$ for visits #1 and 5, respectively.

HST NICMOS slit-less grisms have a number of instrument related systematic effects that appear in precision photometry. These effects include detector wavelength dependancies such as the flat field, sensitivity, PSF, and resolution which interact in a complex manner with telescope's PSF stability and pointing accuracy. With these effects, typical transit programs with HST NICMOS grisms tend to exhibit large intra-orbit flux variations as the telescope thermally relaxes from day-to-night and orbit-to-orbit flux variations largely dependent on the grating filter wheel position and spectral trace (see Figs. 1 and 2 of Carter et al. 2009). In addition, the low resolution Nic 3 camera used for grism observations is highly under-sampled leading to large

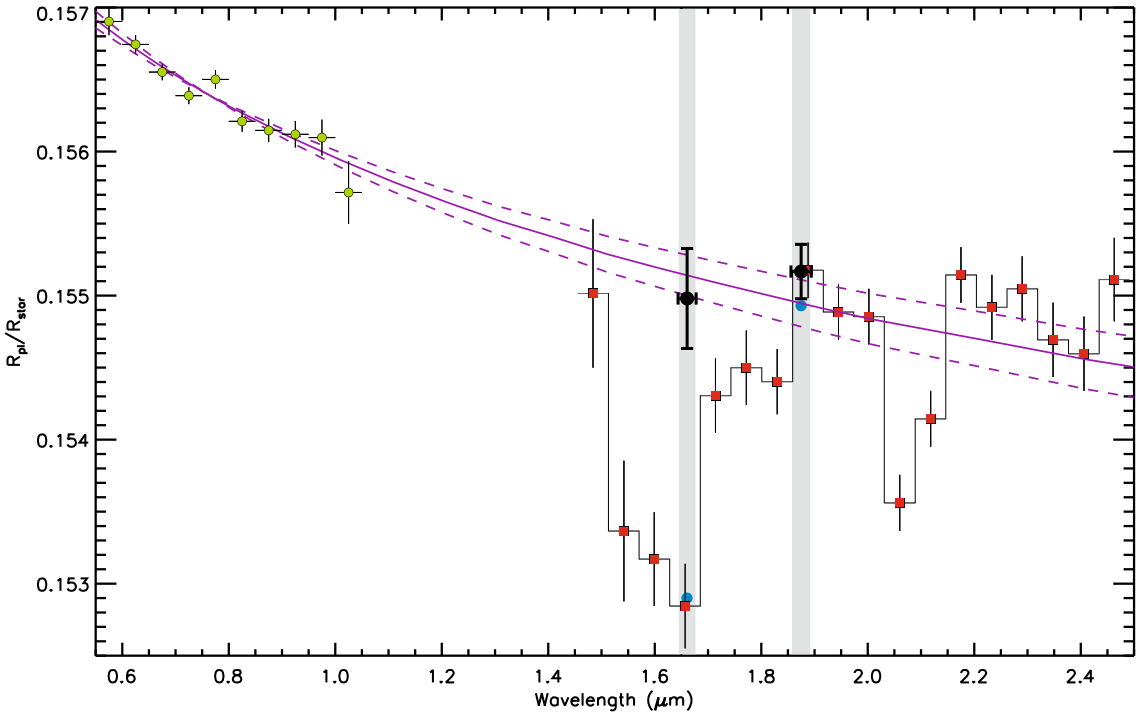

Fig. 6. Measured planetary radii for HD 189733b at optical and near-infrared wavelengths. Plotted are the results from our NICMOS narrowband photometry (black dots), along with the NICMOS grism spectrum (red squares) from Swain et al. (2008), and ACS grism spectrum (green dots) from Pont et al. (2008). The 1-σ error bars on the fit radii are indicated (y-axis error bars), along with the wavelength range of each observation (x-axis error bars, grey vertical bars). Also plotted (purple) is the prediction by Rayleigh scattering due to haze from Lecavelier et al. (2008a), projected here into the near-infrared along with the 1-σ error on the predicted slope (purple, dashed lines). The NICMOS spectrum from Swain et al. (2008) is quoted as being uncertain in its absolute flux level by $\pm 2 \times 10^{-4}$ (± 0.00064 $R_{pl}/R_{\star}$), an offset of -0.00042 $R_{pl}/R_{\star}$ was applied here for comparison reasons such that the values at 1.87 μm match. Our 1.66 μm results are in disagreement with the both the Swain et al. spectra and the expected H_2O atmospheric signature (blue dots), but are in excellent agreement with the predicted planetary radii values from atmospheric haze.

intra-pixel sensitivities, though these can be largely averaged out by defocusing the detector. The importance of systematic errors resulting from the grating filter wheel position on HD 189733b's spectrum can be seen in the emission spectrum from Swain et al. (2009). This spectrum shows nonphysical results (with negative planet fluxes) at the blue-edge of the spectrum. At the edges, the spectral trace has the largest orbit-to-orbit deviations, causing greater systematic errors. The HD 189733b NICMOS transmission and emission spectra were both observed and reduced in much the same manner by Swain et al., thus the edges of the transmission spectra should also be suspect of underestimated uncertainties and greater residual systematic errors.

In a separate NICMOS spectroscopic study of GJ436b by Pont et al. (2008), variations at the 4×10^{-4} flux level in the transmission spectrum were also found, similar in amplitude to the Swain et al. spectral features of HD 189733b. However, given the level of measured systematic errors, Pont et al. (2008) chose not to interpret the GJ436b variations as due to real planetary transmission features, but rather as systematic errors. These errors exhibited a wavelength dependence that was time dependent, with spectral features slowly shifting in wavelength with time, as expected from the HST thermal focus variation systematic effect. While Pont et al. (2008) and Swain et al. (2008) used different NICMOS grisms, both corrected for systematic errors in a similar manner adopting a multilinear decorrelation against external variables including the position, rotation, and width of the spectral trace. Thus, similar systematic errors between the two studies may be expected. A systematic error of 4×10^{-4} in flux would correspond to an error of ~ 0.0013 $R_{pl}/R_{\star}$ at a given wavelength in HD 189733b and ~ 0.0018 $R_{pl}/R_{\star}$ when comparing the difference between two wavelengths, possibly accounting for the features in the Swain et al. (2008) spectrum.

With NICMOS grisms, wavelength shifts and a variable PSF with time can change the flux per pixel with time, which becomes compounded by pixel-to-pixel and sub-pixel response variations which are not accurately known. Observing with narrowband photometric filters mitigates these wavelength dependent and PSF effects, eliminating the need to correct for the systematic errors shown by the grism spectra (a main motivation behind our original selection of narrowband filters). Given our robust (decorrelation free) photometry and the suspect edges of the transmission spectra, the differences between our results and Swain et al. (2008) would clearly seem to favor grism-related systematic errors as the principal cause.

5.3. Atmospheric haze in the near-infrared

Although our results on the planet-to-star radius ratios measured at 1.66 μm and 1.87 μm are significantly different from the Swain et al. (2008) measurements at the same wavelengths, our results are still consistent at both wavelengths with the extrapolation of measurements at optical wavelengths assuming Rayleigh scattering. In effect, the accurate measurements of Pont et al. (2008) showed a significant decrease of the planet radius toward longer wavelengths that was interpreted as the signature of absorption by haze. Lecavelier des Etangs et al. (2008a) showed that the radius variation from 0.55 to 1.05 μm is a signature of the Rayleigh scattering with a decrease of the cross-section

following a λ^{-4} power law. This law can be extrapolated to 1.87 μm. We find that both our measurements at 1.66 μm and 1.87 μm are in excellent agreement with the Rayleigh scattering prediction (Fig. 6). As shown in Lecavelier des Etangs et al. (2008a), the slope of the radius as a function of the wavelength in the Rayleigh regime is characteristic of the atmospheric temperature. The slope for extreme temperatures of 1190 and 1490 K are plotted in Fig. 6 (dotted purple lines). We can see that the smaller slope corresponding to the lowest temperatures is slightly favored, in particular by the 1.87 μm measurement.

We performed a global fit to the present new measurements together with the Pont et al. (2008) published values. With the hypothesis of pure Rayleigh scattering, the data are well fitted with a reduced χ^2 of 1.1 despite the extended width of the spectral domain spread over a factor 4 in wavelength. We find that the temperature given by the Rayleigh power law is 1280 ± 110 K. This temperature agrees with Spitzer 8 and 24 μm phase curve measurements, which also find similar temperatures of $(T_{\rm max} + T_{\rm min})/2 = 1134$ and 1102 K respectively (Knutson et al. 2009). Relaxing the Rayleigh hypothesis and using Mie scattering from 0.55 μm to 1.87 μm, we obtain new constraints on the particle size and their optical properties (see Lecavelier des Etangs et al. 2008a), with the fit to the data slighly improved. Mie scattering implies a larger possible temperature range of 1170 to 1870 K (includes 1σ error) because of a less steep extinction variation with wavelength in the near infrared. The proposed scenario with $MgSiO_3$ still holds, and we find that the particle maximum size must be in the range 0.009 μm to 0.086 μm. Recall that because the Rayleigh scattering cross-section is proportional to the particle size, $a_{\rm part}$, to the power of 6 ($\sigma \propto a_{\rm part}^6$), the size range given above is the size of the largest particles in the size distribution.

Finally, the interpretation of the present transit absorption signatures in terms of Rayleigh scattering at $\lambda \lesssim 2\,\mu$m is consistent with the measurements of emission spectra which do not show signatures of haze absorption. This is explained by the fact that the slant transit geometry probes atmospheres at high altitude and is more sensitive to low absorption cross-sections, while the normal viewing geometry of emission spectra probes deeper in the atmosphere (Fortney 2005). Though more uncertain in the absolute planet-to-star radius contrast, the Swain et al. (2008) transmission spectrum can also be considered as consistent with the haze interpretation if the extreme parts of their absorption spectra are disregarded (Fig. 7).

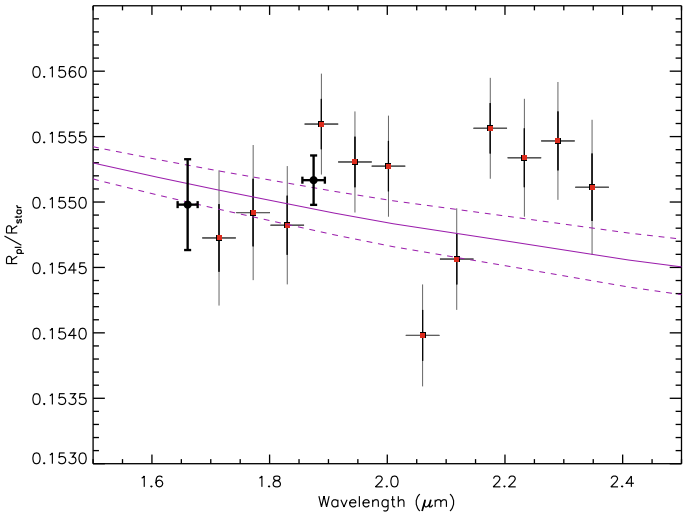

Fig. 7. Similar to Fig. 6, except the Swain et al. (2008) data are plotted at the original unshifted level and the points at the ends of the spectrum (likely affected by systematic errors) are removed. Both 1σ error-bars (thick) and 2σ error-bars (thin) on the Swain et al. spectra are also shown to illustrate that it is consistent at that level with Rayleigh scattering by condensate haze, below 2 μm.

6. Conclusions

Narrow-band NICMOS photometry can provide a robust method for obtaining precision near-infrared photometry. With transiting planets, this can lead to secure near-infrared planetary radii where important molecular and condensate atmospheric planetary signatures can be found. With two carefully selected narrow-band filters, we are able to provide stringent constraints on the presence of H_2O absorption features. We find that upper-atmospheric haze provides sufficient opacity in slant transit geometry to obscure the near-IR H_2O molecular signatures below 2 μm. While absorption due to H_2O was reported by Swain et al. (2008), we rule out any such feature at 5σ and find that their observed feature is likely an artifact of residual systematic errors compromising the spectral edges. The planetary radii values from Pont et al. (2008) and this work indicate that Rayleigh scattering dominates the broadband transmission spectrum from at least 0.5 to 2 μm, with sub-micron $MgSiO_3$ haze particles a probable candidate (Lecavelier des Etangs et al. 2008a). The transition wavelength between the transmission spectra being dominated by haze particles and molecular features would seem to be between 2 and 3 μm, as the IRAC Spitzer photometry between 3 and 8 microns all show planet radii in excess of those predicted by Rayleigh scattering (Désert et al. 2009a,b). To be clear, while our observations rule out detectable quantities of H_2O in the near-IR at these high altitudes, the presence of methane in the Swain et al. transmission spectrum is still possible, though it needs verification, as the 2.2 to 2.4 μm region appears to show an excess absorption over the Rayleigh prediction.

Spectroscopic characterization of transiting planets with JWST NIRCam and NIRSpec are anticipated to make significant contributions to exoplanet science (Deming et al. 2009). These instruments have similar detectors and observing modes as HST NICMOS, with NIRCam also containing similar narrow-band filters to those used here. While the systematic errors observed with HST and Spitzer should be greatly reduced in JWST, the correspondingly greater precisions that will be attempted, as super-Earths are observed, ensure that at some level these systematic errors will likely remain. Strategic use of narrowband filters can provide robust measurements with which to compare atmospheric features seen in transmission or emission spectra, checking both observing methods at key wavelengths. As no upcoming instrument will soon be able to compete with JWST, such independent methods may be the only way to confidently verify groundbreaking results in super-Earth spectra requiring significant systematic error corrections.

Acknowledgements. D.K.S. is supported by CNES. G.E.B. was supported for this work by NASA through grant GO-11117 to the Univ. of Arizona from the STScI. G.W.H. acknowledges long-term support from NASA, NSF, Tennessee State University, and the State of Tennessee through its Centers of Excellence Program. This work is based on observations with the NASA/ESA Hubble Space Telescope, obtained at the Space Telescope Science Institute (STScI) operated by AURA, Inc. We thank the referee F. Pont for the valuable insights into NICMOS grism errors. D.K.S. and G.E.B. would like to thank M. Rieke for valuable discussions regarding the NICMOS instrument. D.K.S. would also like to thank the helpful and knowledgeable staff at STScI for their input in the planning and execution of the observations.

References

Ballester, G. E., Sing, D. K., & Herbert, F. 2007, Nature, 445, 511
Barber, R. J., Tennyson, J., Harris, G. J., & Tolchenov, R. N. 2006, MNRAS, 368, 1087
Bigot, L., Kervella, P., Thévenin, F., & Ségransan, D. 2006, A&A, 446, 635
Bouchy, F., Udry, S., Mayor, M., et al. 2005, A&A, 444, L15
Brown, T. M., Charbonneau, D., Gilliland, R. L., Noyes, R. W., & Burrows, A. 2001, ApJ, 552, 699
Burrows, A., Hubeny, I., Budaj, J., Knutson, H. A., & Charbonneau, D. 2007, ApJ, 668, L171
Carter, J. A., Winn, J. N., Gilliland, R., & Holman, M. J. 2009, ApJ, 696, 241
Charbonneau, D., Brown, T. M., Noyes, R. W., & Gilliland, R. L. 2002, ApJ, 568, 377
Claret, A. 2000, A&A, 363, 1081
Deming, D., Seager, S., Winn, J., et al. 2009, PASP, 121, 952
Désert, J.-M., Vidal-Madjar, A., Lecavelier des Etangs, A., et al. 2008, A&A, 492, 585
Désert, J.-M., Lecavelier des Etangs, A., Hébrard, G., et al. 2009a, ApJ, 699, 478
Désert, J.-M., Sing, D. K., Vidal-Madjar, A., et al. 2009b, A&A, submitted
Fortney, J. J. 2005, MNRAS, 364, 649
Fortney, J. J., Lodders, K., Marley, M. S., & Freedman, R. S. 2008, ApJ, 678, 1419
Grillmair, C. J., Charbonneau, D., Burrows, A., et al. 2007, ApJ, 658, L115
Grillmair, C. J., Burrows, A., Charbonneau, D., et al. 2008, Nature, 456, 767
Hébrard, G., & Lecavelier Des Etangs, A. 2006, A&A, 445, 341
Henry, G. W., & Winn, J. N. 2008, AJ, 135, 68
Hubeny, I., Burrows, A., & Sudarsky, D. 2003, ApJ, 594, 1011
Knutson, H. A., Charbonneau, D., Allen, L. E., et al. 2007, Nature, 447, 183
Knutson, H. A., Charbonneau, D., Allen, L. E., Burrows, A., & Megeath, S. T. 2008, ApJ, 673, 526
Knutson, H. A., Charbonneau, D., Cowan, N. B., et al. 2009, ApJ, 690, 822
Lecavelier des Etangs, A., Pont, F., Vidal-Madjar, A., & Sing, D. 2008a, A&A, 481, L83
Lecavelier des Etangs, A., Vidal-Madjar, A., Désert, J.-M., & Sing, D. 2008b, A&A, 485, 865
Mandel, K., & Agol, E. 2002, ApJ, 580, L171
Moutou, C., Pont, F., Bouchy, F., & Mayor, M. 2004, A&A, 424, L31
Neckel, H., & Labs, D. 1994, Sol. Phys., 153, 91
Pál, A. 2008, MNRAS, 390, 281
Pont, F., Zucker, S., & Queloz, D. 2006, MNRAS, 373, 231
Pont, F., Gilliland, R. L., Moutou, C., et al. 2007, A&A, 476, 1347
Pont, F., Knutson, H., Gilliland, R. L., Moutou, C., & Charbonneau, D. 2008, MNRAS, 385, 109
Pont, F., Gilliland, R. L., Knutson, H., Holman, M., & Charbonneau, D. 2009, MNRAS, 393, L6
Redfield, S., Endl, M., Cochran, W. D., & Koesterke, L. 2008, ApJ, 673, L87
Sing, D. K., Vidal-Madjar, A., Désert, J.-M., Lecavelier des Etangs, A., & Ballester, G. 2008a, ApJ, 686, 658
Sing, D. K., Vidal-Madjar, A., Lecavelier des Etangs, A., et al. 2008b, ApJ, 686, 667
Snellen, I. A. G., Albrecht, S., de Mooij, E. J. W., & Le Poole, R. S. 2008, A&A, 487, 357
Swain, M. R., Vasisht, G., & Tinetti, G. 2008, Nature, 452, 329
Swain, M. R., Vasisht, G., Tinetti, G., et al. 2009, ApJ, 690, L114
Vidal-Madjar, A., Lecavelier des Etangs, A., Désert, J.-M., et al. 2003, Nature, 422, 143
Vidal-Madjar, A., Désert, J.-M., Lecavelier des Etangs, A., et al. 2004, ApJ, 604, L69
Vidal-Madjar, A., Lecavelier des Etangs, A., Désert, J.-M., et al. 2008, ApJ, 676, L57
Winn, J. N., Holman, M. J., Henry, G. W., et al. 2007, AJ, 133, 1828
Zahnle, K., Marley, M. S., Freedman, R. S., Lodders, K., & Fortney, J. J. 2009, ApJ, 701, L20